

# Light-driven CO<sub>2</sub> methanation over Au-grafted Ce<sub>0.95</sub>Ru<sub>0.05</sub>O<sub>2</sub> solid-solution catalysts with activities approaching the thermodynamic limit

Received: 3 February 2022

Accepted: 11 May 2023

Published online: 15 June 2023

 Check for updates

Haoyang Jiang<sup>①</sup>, Linyu Wang<sup>1</sup>, Hiroaki Kaneko<sup>2</sup>, Rongtian Gu<sup>3</sup>, Guangxu Su<sup>4</sup>, Le Li<sup>1</sup>, Jin Zhang<sup>1</sup>, Hucheng Song<sup>5</sup>, Feng Zhu<sup>1</sup>, Akira Yamaguchi<sup>②</sup>, Jun Xu<sup>5</sup>, Fanxin Liu<sup>4</sup>, Masahiro Miyauchi<sup>②</sup>, Weiping Ding<sup>③</sup> & Miao Zhong<sup>①</sup>✉

Photothermal CO<sub>2</sub> methanation offers a clean and sustainable solution to store intermittent renewable energy as synthetic CH<sub>4</sub>. However, its high reaction temperature and low space-time yield hinder its industrial application. Here we report an Au/Ce<sub>0.95</sub>Ru<sub>0.05</sub>O<sub>2</sub> solid-solution catalyst exhibiting a remarkable photothermal CO<sub>2</sub> methanation activity approaching the thermal catalysis limit under visible–near-infrared light irradiation without external heating. Localized surface-plasmon-induced hot-electron injection created abundant oxygen vacancies near the dispersed ruthenium sites, accelerating CO<sub>2</sub> methanation. An approximately 6- to 8-fold increase in the pre-exponential factor was evidenced using Arrhenius plot analysis under visible–near-infrared light irradiation. Using a flow reactor, a photothermal CH<sub>4</sub> production rate of 473 mmol g<sup>-1</sup> cat h<sup>-1</sup> was obtained at a gas hourly space velocity of 80,000 ml g<sup>-1</sup> cat h<sup>-1</sup> with ~100% CH<sub>4</sub> selectivity, ~75% single-pass CO<sub>2</sub> conversion and excellent durability. Our study offers insights into plasmonic-steered photochemistry, which may open opportunities for the high-yielding synthesis of carbon-based chemicals using solar energy.

In the face of global climate change and environmental problems, a growing number of countries have issued plans for carbon emission peaks and carbon neutrality goals, wherein the upgrading of CO<sub>2</sub> into valuable chemicals using solar, wind and hydraulic energy could play a key role in meeting these goals. In this context, the methanation of CO<sub>2</sub> (ref. 1) is particularly attractive because the global CH<sub>4</sub> market continues to rise steadily, and is expected to reach 4–5 trillion m<sup>3</sup> per year by 2030 (ref. 2). Many countries have therefore initiated renewable-powered plans which are expected to produce

4–65 billion m<sup>3</sup> of CH<sub>4</sub> per year from green H<sub>2</sub> and waste CO<sub>2</sub> by 2030 (refs. 2–4).

Although CO<sub>2</sub> methanation is a thermodynamically downhill reaction, substantial energy is required to activate the CO<sub>2</sub> molecule (C=O bond energy, 806 kJ mol<sup>-1</sup>)<sup>1</sup>. In thermal catalysis, the high temperatures required to achieve sufficient reaction rate (typically 300–500 °C)<sup>1</sup> increase implementation expenses, fuel costs and CO<sub>2</sub> emissions.

In contrast, photothermal catalysis, which uses solar energy to generate heat energy on a catalyst surface, is an alternative route to

<sup>1</sup>College of Engineering and Applied Sciences, National Laboratory of Solid State Microstructures, Jiangsu Key Laboratory of Artificial Functional Materials, Nanjing University, Nanjing, China. <sup>2</sup>School of Materials and Chemical Technology, Tokyo Institute of Technology, Tokyo, Japan. <sup>3</sup>School of Chemistry and Chemical Engineering, Nanjing University, Nanjing, China. <sup>4</sup>Department of Applied Physics, Zhejiang University of Technology, Hangzhou, China. <sup>5</sup>School of Electronic Science and Engineering, Nanjing University, Nanjing, China. ✉e-mail: [miaozhong@nju.edu.cn](mailto:miaozhong@nju.edu.cn)

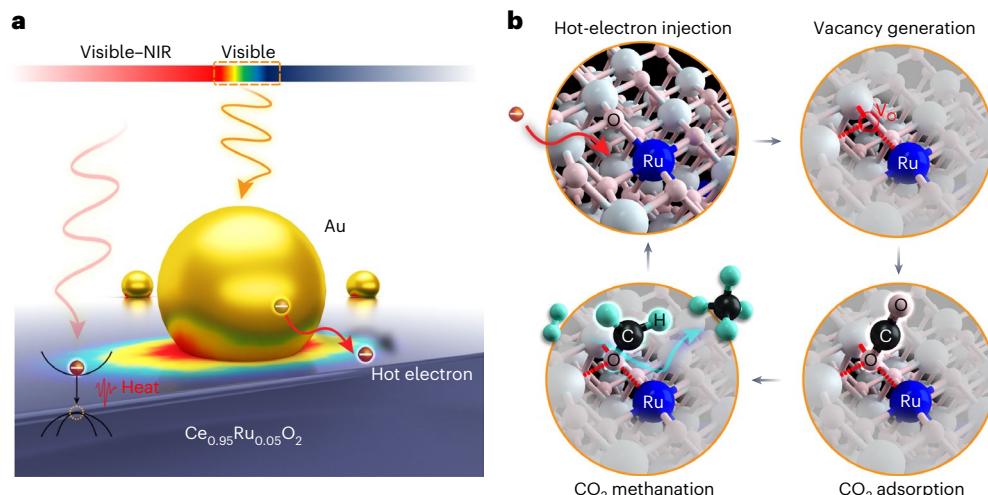


**Fig. 1 | Schematic of photothermal CO<sub>2</sub> methanation over Au/Ce<sub>0.95</sub>Ru<sub>0.05</sub>O<sub>2</sub>.** **a**, The plasmonic-steered photochemical and photothermal synergy. NIR, near-infrared. **b**, The CO<sub>2</sub> methanation process.

offset the strong reliance on fossil fuel energy<sup>5–7</sup>. Typically, catalysts with broad-band light absorption properties, such as iron-based hydro-talcite derivatives<sup>8,9</sup>, Ru/Mg(OH)<sub>2</sub> (ref. 10) and Ni/MXenes<sup>11</sup>, have been examined. However, in all such cases, the temperature was the only driving force for the reaction. In addition, considering that light irradiation is mainly limited to the catalyst surface, only the top 20–100 μm catalyst layers can be used for the reaction<sup>12</sup>, and as a result, the reported photothermal CH<sub>4</sub> space-time yields were much lower than those achieved using thermal catalysis.

Recent studies have proposed that light-induced localized surface plasmon resonance (LSPR) on a catalyst can significantly enhance the reaction activity via a synergistic photothermal and photochemical process. More specifically, Auger recombination of the LSPR-induced hot electrons from Landau damping<sup>13</sup> or electron–phonon interactions provides local heating to the active sites at the metal–catalyst interfaces, increasing the thermal-to-chemical energy efficiency. In addition, some reports have also suggested a photoassisted non-thermal effect<sup>14–20</sup>, wherein the LSPR-induced hot electrons may interact with electrons in the bonding and antibonding states of the adsorbed molecules to reduce the energy barrier in the key steps of the reactions. However, it remains unclear how such LSPR-induced hot electrons, with lifetimes ranging from femtoseconds to picoseconds<sup>21</sup>, are involved in a reaction step that takes place on a timescale of microseconds to milliseconds. In addition, the activities of these LSPR-driven reactions were found to be significantly lower than those obtained under thermal conditions.

We present herein an Au<sub>0.1</sub>/Ce<sub>0.95</sub>Ru<sub>0.05</sub>O<sub>2</sub> catalyst that exhibits a remarkable photothermal catalytic activity in the production of CH<sub>4</sub> from CO<sub>2</sub> without the requirement for external heating. More specifically, Ce<sub>0.95</sub>Ru<sub>0.05</sub>O<sub>2</sub> solid-solution nanorods provide highly dispersed ruthenium sites for CO<sub>2</sub> methanation while serving as a visible–near-infrared light absorber to elevate the catalyst temperature. In addition, gold nanoparticles absorb visible light to generate strong plasmons at the Au<sub>0.1</sub>/Ce<sub>0.95</sub>Ru<sub>0.05</sub>O<sub>2</sub> interfaces. Synchronous illumination X-ray photoelectron spectroscopy (XPS), isotope tracing and electron paramagnetic resonance (EPR) analyses reveal the role of the LSPR-induced hot electrons in the creation of oxygen vacancies (V<sub>0</sub>) and in the enhancement of the photothermal catalytic activity. Furthermore, Arrhenius plots determine an approximately 6- to 8-fold increase in the pre-exponential factor of the reaction rate with Au<sub>0.1</sub>/Ce<sub>0.95</sub>Ru<sub>0.05</sub>O<sub>2</sub> compared with Ce<sub>0.95</sub>Ru<sub>0.05</sub>O<sub>2</sub> under visible–near-infrared light irradiation. In a flow reactor, we obtain a

photothermal catalytic CH<sub>4</sub> production rate of 473 mmol g<sub>cat</sub><sup>-1</sup> h<sup>-1</sup> at a high gas hourly space velocity (GHSV) of 80,000 ml g<sub>cat</sub><sup>-1</sup> h<sup>-1</sup>, surpassing the previously reported state-of-the-art CH<sub>4</sub> space-time yield of 200–300 mmol g<sub>cat</sub><sup>-1</sup> h<sup>-1</sup> at a GHSV of 40,000–60,000 ml g<sub>cat</sub><sup>-1</sup> h<sup>-1</sup> using thermal catalytic fixed-bed reactors<sup>22</sup>. The high photothermal catalytic performance is accompanied by an ~100% CH<sub>4</sub> selectivity and ~75% single-pass CO<sub>2</sub> conversion, approaching the thermodynamic limit of CO<sub>2</sub> methanation. Quantification of the temperature distribution in the catalyst bed under photothermal conditions reveals that only half of the catalyst volume exceeds the CO<sub>2</sub> methanation onset temperature of 250 °C. Therefore, the CH<sub>4</sub> production rate is notably higher (927 mmol g<sub>cat</sub><sup>-1</sup> h<sup>-1</sup>). Additionally, to better characterize the photothermal and photochemical contributions, we develop a screen-printing approach to prepare thin catalyst layers (20–30 μm) on quartz fibre substrates (28 cm<sup>2</sup>) that exhibit notably enhanced photothermal catalytic activities under visible-light irradiation. Finally, Au<sub>0.1</sub>/Ce<sub>0.95</sub>Ru<sub>0.05</sub>O<sub>2</sub> shows excellent durability due to its notable anticoking properties and suppression of ruthenium atom aggregation in stable Ce<sub>0.95</sub>Ru<sub>0.05</sub>O<sub>2</sub> solid solutions across the entire photothermal CO<sub>2</sub> methanation process.

## Results

### Evaluation of the catalytic performance

Figure 1 illustrates the plasmonic-steered photochemical and photothermal synergy for CO<sub>2</sub> methanation over gold-grafted Ce<sub>0.95</sub>Ru<sub>0.05</sub>O<sub>2</sub> catalyst. In this study, Ce<sub>0.95</sub>Ru<sub>0.05</sub>O<sub>2</sub> and Au<sub>m</sub>/Ce<sub>0.95</sub>Ru<sub>0.05</sub>O<sub>2</sub> ( $m = 0.05, 0.075, 0.1, 0.125$  and  $0.15$ ) solid-solution catalysts were synthesized via a one-pot co-precipitation method. The nominal amount of incorporated ruthenium was set as 5 at.%. Initially, model tests were performed to evaluate the CO<sub>2</sub> methanation performances of Ce<sub>0.95</sub>Ru<sub>0.05</sub>O<sub>2</sub> and Au<sub>0.1</sub>/Ce<sub>0.95</sub>Ru<sub>0.05</sub>O<sub>2</sub> in a flow reactor (that is, a Harrick heat chamber; Supplementary Fig. 1) using a mixed gas composition of 72% H<sub>2</sub>, 18% CO<sub>2</sub> and 10% Ar at a GHSV of 50,000 ml g<sub>cat</sub><sup>-1</sup> h<sup>-1</sup>. Before carrying out the tests, the catalysts were pretreated at 400 °C for 20 min at the same gas flow rate.

During thermal catalysis, low CH<sub>4</sub> formation rates of ~0.4 mmol cm<sup>-2</sup> h<sup>-1</sup> were obtained over Ce<sub>0.95</sub>Ru<sub>0.05</sub>O<sub>2</sub> and Au<sub>0.1</sub>/Ce<sub>0.95</sub>Ru<sub>0.05</sub>O<sub>2</sub> at the onset temperature of 250 °C, which is far below the theoretical limit calculated from the thermodynamic equilibrium<sup>23</sup> (dashed line in Fig. 2a). Upon increasing the bulk temperature to 350 °C, the reaction rates of both systems increased rapidly to ~9.7 mmol cm<sup>-2</sup> h<sup>-1</sup>. In contrast, the CH<sub>4</sub> formation rate and CH<sub>4</sub> yield

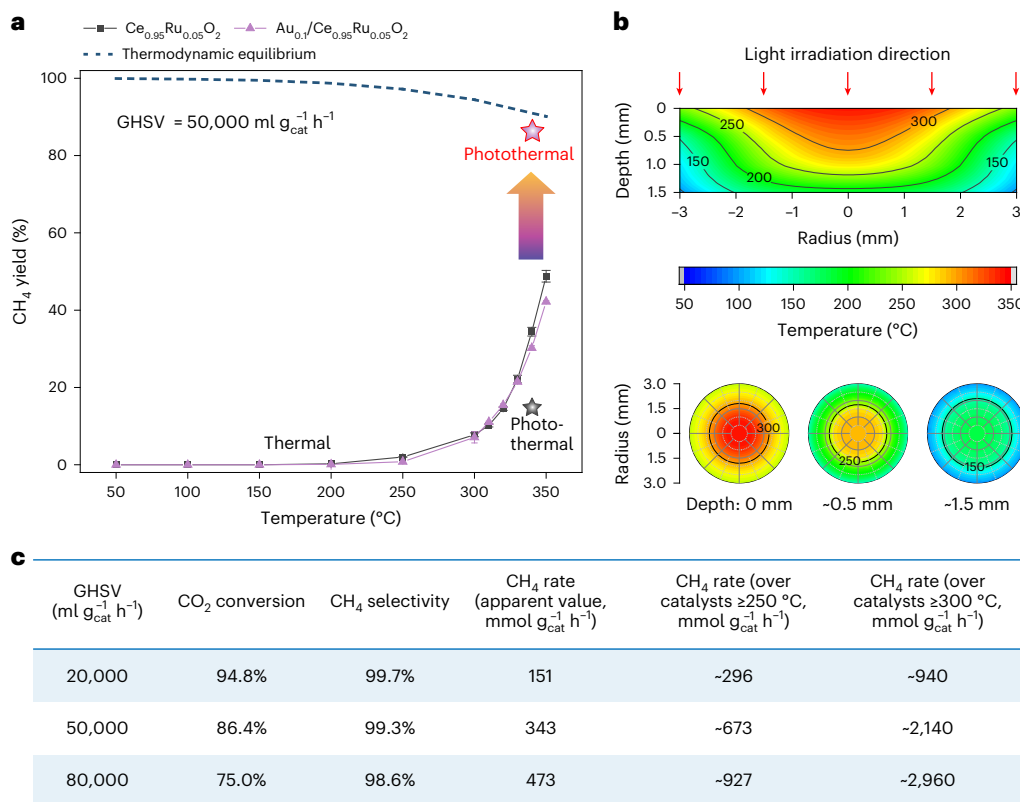


**Fig. 2 | Photothermal and thermal catalytic CO<sub>2</sub> methanation model tests.** **a**, Catalytic activities as a function of temperature in the dark (thermal catalysis) and under 350–2,500 nm light irradiation in a flow reactor without external heating (photothermal catalysis). The temperature represents the catalyst bulk temperature during thermal catalysis and the surface temperature during photothermal catalysis. The same quantity of catalyst was employed to evaluate the photothermal and thermal catalytic performances. Error bars represent

the s.d. based on three measurements. **b**, Temperature distribution in the catalyst bed under the same light irradiation conditions (that is, the highest surface temperature was fixed at 340 °C). **c**, Photothermal CO<sub>2</sub> methanation performance achieved using Au<sub>0.1</sub>/Ce<sub>0.95</sub>Ru<sub>0.05</sub>O<sub>2</sub> at different GHSVs. The corresponding CH<sub>4</sub> production rates are provided considering the catalyst volume at temperatures of ≥250 °C and ≥300 °C in the catalyst bed.

over Au<sub>0.1</sub>/Ce<sub>0.95</sub>Ru<sub>0.05</sub>O<sub>2</sub> were drastically enhanced in the photothermal catalytic process under illumination conditions (350–2,500 nm, 1.6 W/5.3 W cm<sup>-2</sup> from a CME-303 xenon lamp) without external heating. Remarkably, a photothermal catalytic CH<sub>4</sub> formation rate of 17.0 mmol cm<sup>-2</sup> h<sup>-1</sup> was obtained along with an ~86% CH<sub>4</sub> yield, which is approaching the thermodynamic limit of the CO<sub>2</sub> methanation process. Under these irradiation conditions, the surface temperature was ~340 °C, as measured by an infrared radiation thermometer (Supplementary Fig. 2). The temperature at the bottom of the catalyst bed was ~50 °C, as measured by a built-in thermocouple.

To further investigate the temperature gradients in the catalyst bed, we buried commercial thermochromic temperature indicators in different positions throughout the catalyst bed and measured the temperature distribution under the same irradiated surface temperature conditions (Supplementary Note 1 and Supplementary Fig. 3). Subsequently, we plotted the measured isothermal lines of the longitudinal section in the catalyst bed (surface temperature, 340 °C), and as can be seen from Fig. 2b and Supplementary Figs. 4 and 5, the local temperatures in the catalyst bed show a parabolic distribution. Based on a non-linear fitting using a polynomial equation (Supplementary Note 2 and Supplementary Fig. 6) to fit the temperature distributions over the catalyst bed, we estimated that ~51% of the catalyst volume exceeded 250 °C (that is, the onset temperature for CO<sub>2</sub> methanation), while ~16% of the catalyst volume exceeded 300 °C (that is, the temperature at which a measurable reaction rate was first observed). Therefore, considering the real catalyst volume at temperatures of ≥250 °C and ≥300 °C, the CH<sub>4</sub> production rates per

unit mass are 2- to 6-fold higher than the apparent values, respectively (Fig. 2c and Supplementary Table 1). In addition, we also measured the reaction kinetics under the photothermal conditions without temperature gradients in the catalyst bed; these will be discussed in detail below.

The photothermal catalytic CO<sub>2</sub> methanation performances of the different catalysts were then explored (Supplementary Fig. 7a). More specifically, to obtain the intrinsic activities of the catalysts, a low-concentration mixed gas composed of 4% H<sub>2</sub>, 1% CO<sub>2</sub> and 95% Ar was employed to perform the photothermal reactions. It was found that the reference samples (that is, CeO<sub>2</sub> and Au<sub>0.1</sub>/CeO<sub>2</sub>) failed to produce CH<sub>4</sub>, indicating that the ruthenium atoms are the active sites for CH<sub>4</sub> formation. Indeed, CH<sub>4</sub> production over Ce<sub>0.95</sub>Ru<sub>0.05</sub>O<sub>2</sub> reached 0.39 mmol cm<sup>-2</sup> h<sup>-1</sup> with an 18.0% CO<sub>2</sub> conversion and an 80.8% CH<sub>4</sub> selectivity. Following the grafting of gold onto Ce<sub>0.95</sub>Ru<sub>0.05</sub>O<sub>2</sub> to give the Au<sub>0.1</sub>/Ce<sub>0.95</sub>Ru<sub>0.05</sub>O<sub>2</sub> catalyst, the highest CH<sub>4</sub> formation rate of 0.94 mmol cm<sup>-2</sup> h<sup>-1</sup> was achieved, in addition to a 34.8% CO<sub>2</sub> conversion and a 98.7% CH<sub>4</sub> selectivity. As monitored by an infrared radiation thermometer, the surface temperatures of the Ce<sub>0.95</sub>Ru<sub>0.05</sub>O<sub>2</sub> and Au<sub>0.1</sub>/Ce<sub>0.95</sub>Ru<sub>0.05</sub>O<sub>2</sub> catalysts under identical illumination conditions (350–2,500 nm, 1 W/3.3 W cm<sup>-2</sup> from a CME-303 xenon lamp) were 341 °C and 335 °C, respectively, and so it appeared that the elevated temperatures were mainly due to light absorption at the Ru<sup>n+</sup> defect sites in Ce<sub>0.95</sub>Ru<sub>0.05</sub>O<sub>2</sub> rather than LSPR absorption at the gold nanoparticles (Fig. 1), which agrees with the previous studies that the temperature at the gold–substrate interface does not notably increase (<100 °C) under intensive light illumination (for example, 800 W cm<sup>-2</sup><sup>24–26</sup>. More details

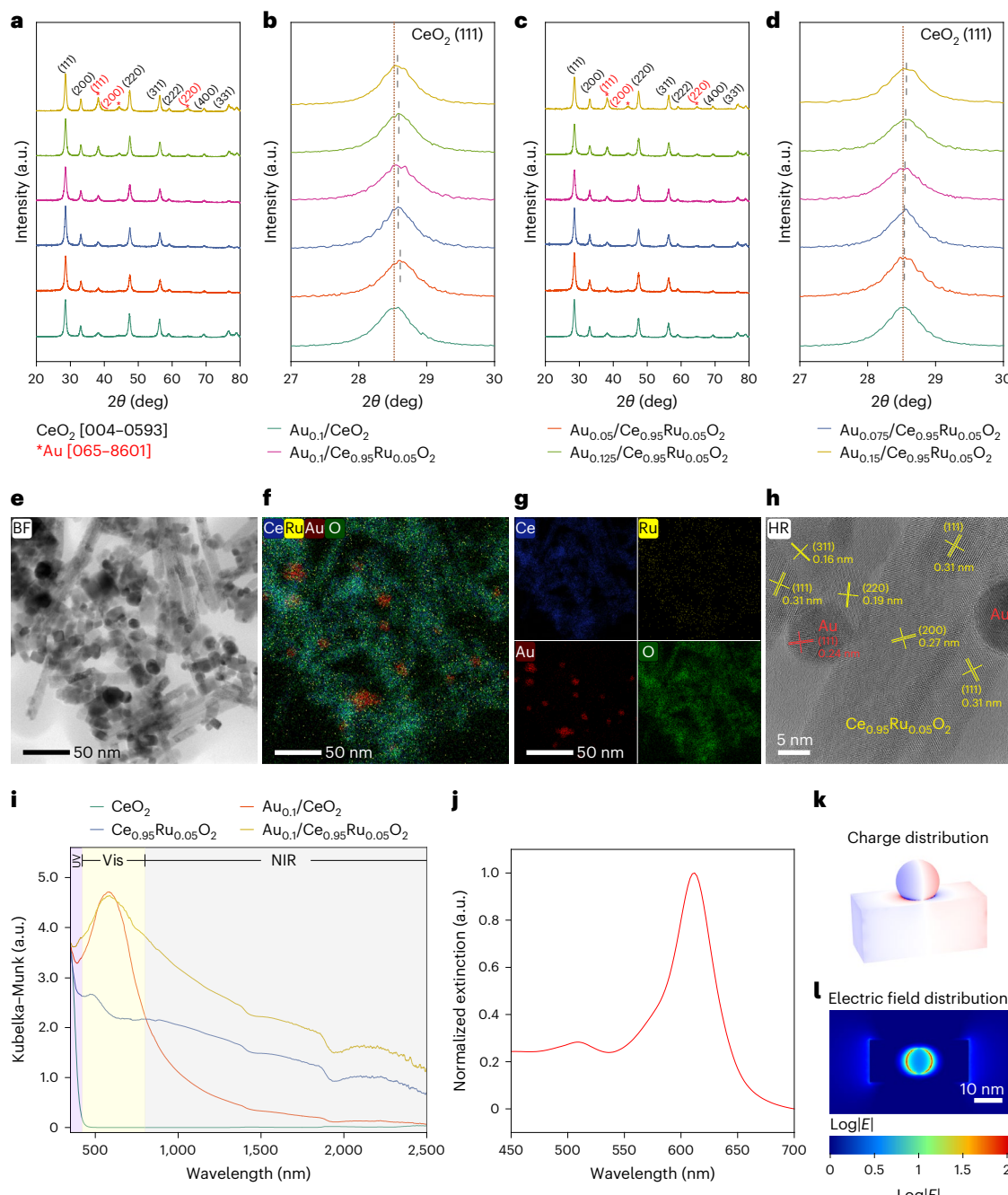


**Fig. 3 | Characterizations.** **a-d**, X-ray diffraction patterns of the  $\text{Au}_m/\text{Ce}_{0.95}\text{Ru}_{0.05}\text{O}_2$  and  $\text{Au}_{0.1}/\text{CeO}_2$  catalysts before (**a**,**b**) and after (**c**,**d**) the reaction. The vertical dashed lines in **b**,**d** indicate the peak positions of  $\text{CeO}_2$ (111) in each sample. The numbers in the square brackets in the **a-d** legend represent the International Center for Diffraction Data card numbers. **e-h**, STEM and TEM images of the  $\text{Au}_{0.1}/\text{Ce}_{0.95}\text{Ru}_{0.05}\text{O}_2$  catalysts after the reaction: bright field (BF)-STEM image (**e**), STEM-EDX mappings of cerium, ruthenium, gold and oxygen (**f**), STEM-EDX mapping overlay image of these elements (**f**) and high-resolution (HR)-TEM image (**h**). **i**, Ultraviolet-visible–near-infrared DRS of the  $\text{CeO}_2$ ,  $\text{Au}_{0.1}/\text{CeO}_2$ ,  $\text{Ce}_{0.95}\text{Ru}_{0.05}\text{O}_2$  and  $\text{Au}_{0.1}/\text{Ce}_{0.95}\text{Ru}_{0.05}\text{O}_2$  catalysts. The Kubelka–Munk values were calculated by the equation  $(1-R^2)/2R$ , where  $R$  is the reflectance. **j-l**, Electromagnetic simulations: simulated extinction spectra (**j**) with the spatial distribution of the charge (**k**) and the electric field (**l**) on the gold-grafted  $\text{CeO}_2$  surfaces under visible light (615 nm) irradiation.

of the evaluation of photothermal catalytic performance are summarized in Supplementary Note 3 and Supplementary Figs. 7–10.

### Characterization

Figure 3a shows the X-ray diffractions patterns of the gold-grafted  $\text{CeO}_2$  and  $\text{Ce}_{0.95}\text{Ru}_{0.05}\text{O}_2$  catalysts, wherein the diffraction peaks at  $38.2^\circ$ ,  $44.4^\circ$  and  $64.6^\circ$  can be attributed to the (111), (200) and (220) lattice planes of gold, respectively. In addition, the intense diffraction peaks

at  $28.5^\circ$ ,  $33.1^\circ$ ,  $47.5^\circ$  and  $56.4^\circ$  correspond to the (111), (200), (220) and (311) lattice planes of fluorite-type  $\text{CeO}_2$ , and hence these results indicate that  $(\text{CeO}_2)_{0.95}(\text{RuO}_2)_{0.05}$  solid solutions were formed for the various  $\text{Au}_m/\text{Ce}_{0.95}\text{Ru}_{0.05}\text{O}_2$  catalysts. Compared with  $\text{Au}_{0.1}/\text{CeO}_2$ , the peak positions of the  $\text{Au}_m/\text{Ce}_{0.95}\text{Ru}_{0.05}\text{O}_2$  (111) planes shifted by  $-0.06^\circ$ – $0.09^\circ$  to higher values of  $2\theta$  (Fig. 3b). This was attributed to the smaller ionic radii of ruthenium ( $\text{Ru}^{3+}$ , 68 pm;  $\text{Ru}^{4+}$ , 62 pm) compared with those of cerium ( $\text{Ce}^{3+}$ , 102 pm;  $\text{Ce}^{4+}$ , 87 pm)<sup>27</sup>; the partial replacement

of cerium with ruthenium ions therefore shrinks the lattice spacing within the  $\text{CeO}_2$  structure. Moreover, the possibility of the interstitial insertion of ruthenium ions cannot be completely ruled out from the X-ray diffraction patterns due to the fact that it exhibits only a minor influence on the lattice spacing. No apparent changes were observed in the X-ray diffraction patterns of the  $\text{Au}_{0.1}/\text{CeO}_2$ ,  $\text{Ce}_{0.95}\text{Ru}_{0.05}\text{O}_2$  and  $\text{Au}_{0.1}/\text{Ce}_{0.95}\text{Ru}_{0.05}\text{O}_2$  catalysts after the  $\text{CO}_2$  methanation reaction (Fig. 3c,d and Supplementary Fig. 11), indicating that the ruthenium atoms remain at the cationic states of the  $\text{CeO}_2$  lattices during the reaction, and are not reduced to metallic  $\text{Ru}^0$ .

Scanning electron microscopy (SEM) images of  $\text{Au}_{0.1}/\text{Ce}_{0.95}\text{Ru}_{0.05}\text{O}_2$  (Supplementary Fig. 12) show a distinct  $\text{CeO}_2$  nanorod morphology. According to the results of energy-dispersive X-ray spectroscopy (EDX) (Supplementary Fig. 13), the amount of ruthenium was determined to be 4.6 at.%, which is close to the 5 at.% of  $\text{RuCl}_3$  used during catalyst preparation. In addition, transmission electron microscopy (TEM) and scanning transmission electron microscopy (STEM) images coupled with EDX elemental mapping revealed gold nanospheres immobilized on the  $\text{Ce}_{0.95}\text{Ru}_{0.05}\text{O}_2$  nanorods. No obvious change in the morphology was observed for the catalysts before and after the reaction (Fig. 3e–h and Supplementary Figs. 14–17), and STEM-EDX elemental mapping (Fig. 3f,g, and Supplementary Fig. 16) illustrated that the ruthenium species were highly dispersed within the  $\text{Ce}_{0.95}\text{Ru}_{0.05}\text{O}_2$  nanorods. Furthermore, high-resolution (HR)-TEM images (Fig. 3h and Supplementary Fig. 15) show lattice fringes with *d* spacings of 0.31, 0.27, 0.19 and 0.16 nm, corresponding to the (111), (200), (220) and (311) lattice planes of the  $\text{Ce}_{0.95}\text{Ru}_{0.05}\text{O}_2$  phase. Lattice fringes with a *d* spacing of 0.24 nm were also observed, corresponding to the (111) lattice plane of the gold nanoparticles. No peaks corresponding to ruthenium or the  $\text{RuO}_x$  nanoparticles were observed, thereby indicating that the ruthenium ions were incorporated into the  $\text{CeO}_2$  lattice structures.

Figure 3i and Supplementary Fig. 18 show the UV-visible-near-infrared diffuse reflectance spectra (DRS) of representative samples. More specifically,  $\text{CeO}_2$  exhibits bandgap absorption in the ultraviolet region, while the  $\text{Ce}_{0.95}\text{Ru}_{0.05}\text{O}_2$  solid solution shows full-spectrum absorption up to 2,500 nm, which is attributed to the impurity absorption arising from the unfilled 4d orbitals of the ruthenium dopants. Both  $\text{Au}_{0.1}/\text{CeO}_2$  and  $\text{Au}_{0.1}/\text{Ce}_{0.95}\text{Ru}_{0.05}\text{O}_2$  presented intense LSPR absorption peaks at ~585 nm in the visible region, and electromagnetic simulations showed an LSPR peak at 612 nm (Fig. 3j), thereby agreeing with the measured ultraviolet-visible-near-infrared spectra. Under irradiation by 615 nm light, the simulated local electromagnetic field at the Au– $\text{CeO}_2$  interface was intensified >100-fold (Fig. 3k,l), which suggested the generation of hot electrons within the gold nanoparticles and their subsequent injection into the  $\text{Ce}_{0.95}\text{Ru}_{0.05}\text{O}_2$  catalyst.

### Photothermal catalytic mechanism

To study the mechanism of the photothermal catalytic  $\text{CO}_2$  methanation reaction, the Arrhenius plots of  $\text{Au}_{0.1}/\text{Ce}_{0.95}\text{Ru}_{0.05}\text{O}_2$  and  $\text{Ce}_{0.95}\text{Ru}_{0.05}\text{O}_2$  were constructed under equivalent reaction conditions. No noticeable changes were observed in the apparent activation energies ( $E_a$ ) of these two catalysts, that is,  $75.1 \pm 2.2 \text{ kJ mol}^{-1}$  for  $\text{Au}_{0.1}/\text{Ce}_{0.95}\text{Ru}_{0.05}\text{O}_2$  and  $71.6 \pm 1.6 \text{ kJ mol}^{-1}$  for  $\text{Ce}_{0.95}\text{Ru}_{0.05}\text{O}_2$  (Fig. 4a), indicating that LSPR-induced hot-electron injection does not reduce the reaction energy. Interestingly, an ~8-fold increase in the pre-exponential factor was observed in the Arrhenius plot, that is,  $0.387 \text{ mol s}^{-1}$  for  $\text{Au}_{0.1}/\text{Ce}_{0.95}\text{Ru}_{0.05}\text{O}_2$  compared with  $0.048 \text{ mol s}^{-1}$  for  $\text{Ce}_{0.95}\text{Ru}_{0.05}\text{O}_2$  under identical conditions. This agrees with the previous study in thermal catalysis that when the two catalysts have almost the same apparent activation energy, the difference in the reaction rates is due to the difference in the number of active sites, that is, the different pre-exponential factors in the Arrhenius equation<sup>28</sup>. In the present study, this increase in the pre-exponential factor implies that there are more active sites present on the  $\text{Au}_{0.1}/\text{Ce}_{0.95}\text{Ru}_{0.05}\text{O}_2$  catalyst upon light irradiation, leading us to

believe that hot-electron injection from gold to  $\text{Ce}_{0.95}\text{Ru}_{0.05}\text{O}_2$  generates an increased number of oxygen vacancies near the ruthenium sites, and these Ru– $\text{V}_o$  active centres accelerate the  $\text{CO}_2$  methanation process, which agrees with the previous studies of the interaction between plasmonic hot electrons and nearby oxygen vacancies<sup>29–31</sup>. In addition, we generated Arrhenius plots of the catalysts without temperature gradients in the catalyst bed under irradiation, confirming that the pre-exponential factor is ~6-fold higher after gold loading (further details are listed in Supplementary Fig. 19). As shown in Fig. 4b, an 8–10 times increase in the pre-exponential factor of the reaction rate equation corresponds to a 15–20% decrease in the overall activation energy, which is significant from the perspective of the reaction microkinetics at a molecular level.

To confirm the proposed mechanism, synchronous illumination XPS was performed<sup>32</sup>. More specifically, under visible-light irradiation (420–780 nm), a clear reduction in the ruthenium valence states to lower than +3 was observed for both  $\text{Ce}_{0.95}\text{Ru}_{0.05}\text{O}_2$  and  $\text{Au}_{0.1}/\text{Ce}_{0.95}\text{Ru}_{0.05}\text{O}_2$ . Furthermore, the binding energies of  $\text{Ru 3p}_{3/2}$  shifted to 462.3–462.4 eV under irradiation, which are lower than those of  $\text{Ru 3p}_{3/2}$  (that is, 463.2–463.3 eV) for the sample before irradiation, and lower than that of  $\text{Ru 3p}_{3/2}$  (that is, 462.8 eV) in the reference sample of Ru(III) 2,4-pentanedionate ( $\text{Ru(acac)}_3$ ). These values are also higher than that of  $\text{Ru 3p}_{3/2}$  (that is, 461.6 eV) in metallic  $\text{Ru}^0$  (Fig. 4c and Supplementary Fig. 20). To further clarify the chemical states of ruthenium in  $\text{Ce}_{0.95}\text{Ru}_{0.05}\text{O}_2$  and  $\text{Au}_{0.1}/\text{Ce}_{0.95}\text{Ru}_{0.05}\text{O}_2$ , we analysed the XPS spectra of the Ru 3d orbitals with a higher signal-to-noise ratio (Fig. 4d). Gold and carbon signals were used as internal standards for calibration and to confirm the ruthenium positions (Fig. 4d and Supplementary Fig. 21d). Prior to light irradiation, we observed split  $\text{Ru}^{4+} 3d_{5/2}$  and  $\text{Ru}^{3+} 3d_{5/2}$  signals at -282.3 and 281.3 eV for both samples, respectively, thereby indicating the proportion of  $\text{Ru}^{4+}$  to be ~80%. Under irradiation, the  $\text{Ru 3d}_{5/2}$  signals shifted to lower binding energies, and the new split peak at -280.4 eV was attributed to  $\text{Ru}^{2+} 3d_{5/2}$  (ref. 33.). Overall, we observed that the  $\text{Au}_{0.1}/\text{Ce}_{0.95}\text{Ru}_{0.05}\text{O}_2$  sample showed a notably higher  $\text{Ru}^{2+}/\text{Ru}^{3+}$  proportion than that of the pristine  $\text{Ce}_{0.95}\text{Ru}_{0.05}\text{O}_2$  (Supplementary Table 2), verifying that the plasmonic hot-electron injection from gold nanoparticles generated a greater number of Ru– $\text{V}_o$  centres. Therefore, the hot-electron injection contributes to the photothermal reaction.

The EPR spectra of  $\text{Au}_{0.1}/\text{Ce}_{0.95}\text{Ru}_{0.05}\text{O}_2$  and  $\text{Ce}_{0.95}\text{Ru}_{0.05}\text{O}_2$  were then compared before and after the photothermal reaction. More specifically, the EPR sampling tube was filled with the desired  $\text{Au}_{0.1}/\text{Ce}_{0.95}\text{Ru}_{0.05}\text{O}_2$  or  $\text{Ce}_{0.95}\text{Ru}_{0.05}\text{O}_2$  catalyst (50 mg) and the photothermal reaction was conducted under visible-light irradiation (420–780 nm) over 40 min; EPR analysis was then carried out. As shown in Fig. 4e,f, the EPR signals at  $g \approx 2.035$  and 2.013 correspond to the typical paramagnetic  $\text{O}_2^-$  species of  $\text{O}_2$  molecules adsorbed on oxygen vacancies<sup>34</sup>. In the case of the pristine  $\text{Ce}_{0.95}\text{Ru}_{0.05}\text{O}_2$ , an increased paramagnetic  $\text{O}_2^-$  signal intensity was observed after  $\text{H}_2$  thermal activation at 400 °C, and this signal did not change after the photothermal reaction, indicating that all the oxygen vacancies were generated from the thermal reduction of  $\text{Ce}_{0.95}\text{Ru}_{0.05}\text{O}_2$  by  $\text{H}_2$ . In the case of  $\text{Au}_{0.1}/\text{Ce}_{0.95}\text{Ru}_{0.05}\text{O}_2$ , the intensity of the paramagnetic  $\text{O}_2^-$  peak further increased 1.3-fold after visible-light illumination. Thus, it was apparent that abundant oxygen vacancies were generated on the  $\text{Au}_{0.1}/\text{Ce}_{0.95}\text{Ru}_{0.05}\text{O}_2$  catalyst under visible-light illumination, and that this number of vacancies was even greater than that created in the  $\text{Ce}_{0.95}\text{Ru}_{0.05}\text{O}_2$  bulk after reduction treatment at 400 °C.

Subsequently, isotopic tracing was employed to provide evidence of the photothermal reaction pathways involved in the  $\text{Ce}_{0.95}\text{Ru}_{0.05}\text{O}_2$  and  $\text{Au}_{0.1}/\text{Ce}_{0.95}\text{Ru}_{0.05}\text{O}_2$  systems. Initially,  $\text{H}_2^{18}\text{O}$  was employed as an  $^{18}\text{O}$  source to substitute some of the lattice oxygen species on the surfaces of  $\text{Ce}_{0.95}\text{Ru}_{0.05}\text{O}_2$  and  $\text{Au}_{0.1}/\text{Ce}_{0.95}\text{Ru}_{0.05}\text{O}_2$  via a thermal treatment process<sup>35</sup>. The photothermal reactions were then performed in a flow reaction system under light irradiation (350–2,500 nm) without

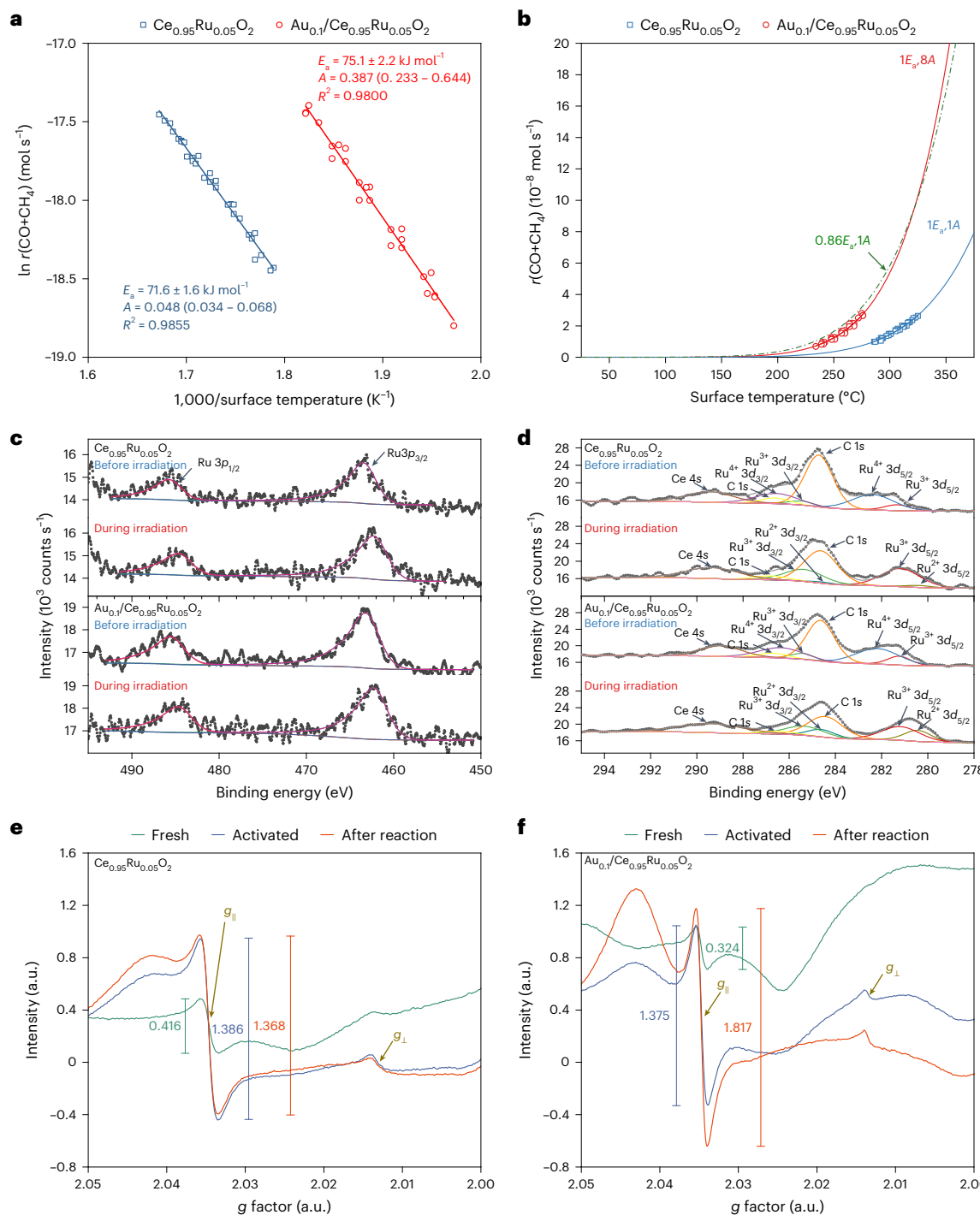


**Fig. 4 | Mechanistic studies.** **a,b**, Arrhenius plots of the  $\text{CO}_2$  methanation process over the  $\text{Ce}_{0.95}\text{Ru}_{0.05}\text{O}_2$  and  $\text{Au}_{0.1}/\text{Ce}_{0.95}\text{Ru}_{0.05}\text{O}_2$  catalysts under 350–2,500 nm light irradiation: calculation of the apparent activation energies ( $E_a$ ) and pre-exponential factors ( $A$ ) for  $\text{CO}_2$  reduction (**a**), and the fitted reaction rates using the Arrhenius equation (**b**).  $R^2$  is the coefficient of determination of the fittings in

a using a linear regression model. **c,d**, Synchronous illumination XPS analysis of the Ru  $3p$  (**c**) and Ru  $3d$  (**d**) signals in  $\text{Ce}_{0.95}\text{Ru}_{0.05}\text{O}_2$  and  $\text{Au}_{0.1}/\text{Ce}_{0.95}\text{Ru}_{0.05}\text{O}_2$  under 420–780 nm light irradiation. **e,f**, EPR analyses of  $\text{Ce}_{0.95}\text{Ru}_{0.05}\text{O}_2$  (**e**) and  $\text{Au}_{0.1}/\text{Ce}_{0.95}\text{Ru}_{0.05}\text{O}_2$  (**f**) before and after the photothermal reaction under 420–780 nm light irradiation.

external heating. The output gas was analysed using an online quadrupole mass spectrometry (QMS) system. As shown in Fig. 5, signals corresponding to  $\text{CO}^{18}\text{O}$  ( $m/z = 46$ ) and  $\text{C}^{18}\text{O}_2$  ( $m/z = 48$ ) were clearly observed upon light irradiation in the presence of the  $^{18}\text{O}$ -substituted  $\text{Au}_{0.1}/\text{Ce}_{0.95}\text{Ru}_{0.05}\text{O}_2$  (red lines) and  $\text{Ce}_{0.95}\text{Ru}_{0.05}\text{O}_2$  catalysts (blue lines). These observations indicate a rapid exchange between  $\text{CO}_2$  and the lattice  $^{18}\text{O}$  species due to the adsorption/desorption of  $\text{CO}_2$  molecules at the surface oxygen vacancies, and subsequent carbonate

transformation upon irradiation<sup>36</sup>. Peaks corresponding to  $\text{H}_2^{18}\text{O}$  ( $m/z = 20$ ) and  $\text{C}^{18}\text{O}$  ( $m/z = 29$ ) were also detected in the catalytic products (Supplementary Fig. 22), thereby indicating that the oxygen vacancies are the primary sites for  $\text{CO}_2$  activation and hydrogenation. In control experiments, no  $^{18}\text{O}$  species were detected under these photothermal conditions using the undoped  $\text{Au}_{0.1}/\text{Ce}_{0.95}\text{Ru}_{0.05}\text{O}_2$  catalyst (green lines) (Fig. 5 and Supplementary Fig. 22), thereby confirming that our isotope experiments were conducted correctly. Furthermore,

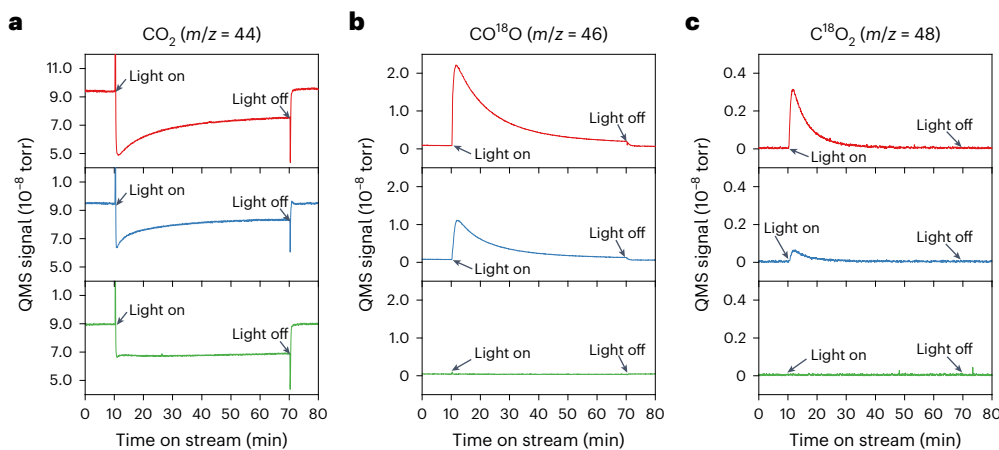


**Fig. 5 | Isotopic trace experiments.** **a–c,** The time-on-stream QMS signals of  $\text{CO}_2$  (**a**),  $\text{CO}^{18}\text{O}$  (**b**) and  $\text{C}^{18}\text{O}_2$  (**c**) during the photothermal reaction under 350–2,500 nm light irradiation for the  $^{18}\text{O}$ -substituted  $\text{Au}_{0.1}/\text{Ce}_{0.95}\text{Ru}_{0.05}\text{O}_2$  (red lines),  $^{18}\text{O}$ -substituted  $\text{Ce}_{0.95}\text{Ru}_{0.05}\text{O}_2$  (blue lines) and isotope-unsubstituted  $\text{Au}_{0.1}/\text{Ce}_{0.95}\text{Ru}_{0.05}\text{O}_2$  (green lines) catalysts.

it was determined quantitatively that the amount of generated  $^{18}\text{O}$  species was notably higher in the case of the  $^{18}\text{O}$ -substituted  $\text{Au}_{0.1}/\text{Ce}_{0.95}\text{Ru}_{0.05}\text{O}_2$  than for the  $^{18}\text{O}$ -substituted  $\text{Ce}_{0.95}\text{Ru}_{0.05}\text{O}_2$ , and this result agrees with the XPS, EPR and Arrhenius plot results to confirm the presence of increased oxygen vacancies on the  $\text{Au}_{0.1}/\text{Ce}_{0.95}\text{Ru}_{0.05}\text{O}_2$  catalyst under irradiation conditions.

We also carried out operando diffuse reflectance infrared Fourier transform spectroscopy (DRIFTS) analysis to identify the intermediate adsorption species in the  $\text{Au}_{0.1}/\text{Ce}_{0.95}\text{Ru}_{0.05}\text{O}_2$  system (Supplementary Fig. 23). More specifically,  $\nu(\text{C=O})$  stretching peaks were observed at  $\sim 2,080$ – $1,950\text{ cm}^{-1}$ , which were attributed to the adsorption of  $\text{CO}_2$  on oxygen vacancies. This  $\nu(\text{C=O})$  stretching was further validated by the online QMS system (Supplementary Fig. 24), wherein a set of  $\nu(\text{C–H})$  and  $\nu(\text{O–C–O})$  stretching peaks were observed at  $2,840$ ,  $1,583$  and  $1,371\text{ cm}^{-1}$ , indicating the generation of formate species during the photothermal catalytic methanation process. We therefore propose that a formate pathway in which the direct hydrogenation of the adsorbed  $\text{CO}_2$  on the Ru– $\text{V}_0$  catalytic sites is predominant during  $\text{CO}_2$  methanation<sup>37</sup> (Supplementary Fig. 25).

Based on these results, we therefore proposed a photothermal-initiated and plasmonic-enhanced  $\text{CO}_2$  methanation mechanism over the gold-grafted  $\text{Ce}_{0.95}\text{Ru}_{0.05}\text{O}_2$  catalyst. More specifically, defective  $\text{Ce}_{0.95}\text{Ru}_{0.05}\text{O}_2$  solid solutions absorb visible–near-infrared light to increase the catalyst temperature, while the gold nanoparticles absorb visible light to excite LSPR hot electrons. The subsequent injection of hot electrons from gold to  $\text{Ce}_{0.95}\text{Ru}_{0.05}\text{O}_2$  creates large quantities of surface oxygen vacancies on the catalyst surface, and these Ru– $\text{V}_0$  active sites stimulate  $\text{H}_2$  dissociation and  $\text{CO}_2$  methanation to drastically promote the photothermal catalytic production of  $\text{CH}_4$  over  $\text{Au}_{0.1}/\text{Ce}_{0.95}\text{Ru}_{0.05}\text{O}_2$  at low bulk temperatures. The proposed concept of injecting plasmonic hot electrons into the neighbouring catalyst to alter its physical or chemical characteristics is in line with previous findings<sup>38–41</sup>. In addition, we carried out a series of control experiments by preventing LSPR excitation or hot-electron transfer, as shown in Supplementary Note 4. Under the same photothermal conditions without hot electron injection, the photothermal catalytic performance notably decreased, thereby suggesting that plasmonic hot-electron injection created a large number of surface active sites to promote the photothermal catalytic activity. This result is in line with the XPS, EPR, isotope and Arrhenius plot analysis, supporting our proposed mechanism.

### Perspectives for practical application

Finally, the photothermal catalytic performance of  $\text{Au}_{0.1}/\text{Ce}_{0.95}\text{Ru}_{0.05}\text{O}_2$  was evaluated using the same gas composition employed for the

thermocatalytic  $\text{CO}_2$  methanation process (that is, 72%  $\text{H}_2$ , 18%  $\text{CO}_2$  and 10% Ar)<sup>42</sup> under light irradiation (350–2,500 nm,  $1.6\text{ W}/5.3\text{ W cm}^{-2}$  from a CME-303 xenon lamp). As shown in Fig. 6a, at a GHSV of  $20,000\text{ ml g}_{\text{cat}}^{-1}\text{ h}^{-1}$ , our photothermal catalytic  $\text{CH}_4$  selectivity reached 99.7%, while a  $\text{CO}_2$  conversion of 94.8% was achieved, and the  $\text{CH}_4$  formation rate was  $7.5\text{ mmol cm}^{-2}\text{ h}^{-1}$ . Notably, at a GHSV of  $80,000\text{ ml g}_{\text{cat}}^{-1}\text{ h}^{-1}$ , the photothermal catalytic  $\text{CH}_4$  selectivity and  $\text{CO}_2$  conversion of this system remained high, with values of 98.6% and 75.0% being recorded, respectively. Moreover, the  $\text{CH}_4$  formation rate reached  $23.5\text{ mmol cm}^{-2}\text{ h}^{-1}$ . It was also confirmed that the gold-grafted sample was superior to  $\text{Ce}_{0.95}\text{Ru}_{0.05}\text{O}_2$  at all GHSVs from 20,000 to  $80,000\text{ ml g}_{\text{cat}}^{-1}\text{ h}^{-1}$  under identical irradiation conditions (Supplementary Fig. 26). Following conversion of the  $\text{CH}_4$  formation rate to  $\text{mmol g}_{\text{cat}}^{-1}\text{ h}^{-1}$  (the third y axis in Fig. 6a), it was compared with previous systems. Significantly, an extremely high reaction rate of  $473\text{ mmol g}_{\text{cat}}^{-1}\text{ h}^{-1}$  (that is,  $23.5\text{ mmol cm}^{-2}\text{ h}^{-1}$  at a GHSV of  $80,000\text{ ml g}_{\text{cat}}^{-1}\text{ h}^{-1}$ ) was obtained. As shown in the temperature distribution measurement, only  $\sim 50\%$  of the catalyst bed exceeds the onset temperature of  $250^\circ\text{C}$ ; therefore, when considering the catalyst volume at a temperature  $\geq 250^\circ\text{C}$ , the  $\text{CH}_4$  production rate was determined to be at least  $927\text{ mmol g}_{\text{cat}}^{-1}\text{ h}^{-1}$  (Supplementary Table 3). The photothermal catalyst appears to outperform previously reported thermal and photocatalytic/photothermal  $\text{CO}_2$  methanation catalysts and systems (Fig. 6c, Supplementary Table 4 and refs. 5, 6, 43–51). The maximum  $\text{CH}_4$  selectivity and  $\text{CO}_2$  conversion also appear to be higher than those of the previously best-performing thermal catalysts (Fig. 6b, Supplementary Table 5 and refs. 22, 37, 42, 52–62). Importantly, it should be noted here that this photothermal catalytic performance was obtained at a moderate bulk temperature of  $\sim 50^\circ\text{C}$  without any external heating, which is notably lower than the temperature required for industrialized fixed-bed reactors (that is,  $300$ – $400^\circ\text{C}$ ), thereby further indicating the potential advantages of the LSPR-hot-electron-enhanced photothermal  $\text{CO}_2$  methanation reaction over conventional energy-intensive thermal systems.

Over five cycles and 10 h of operation, the high  $\text{CH}_4$  selectivity,  $\text{CO}_2$  conversion and  $\text{CH}_4$  formation rate remained stable (Fig. 6d), and TEM analysis confirmed a stable  $\text{Au}_{0.1}/\text{Ce}_{0.95}\text{Ru}_{0.05}\text{O}_2$  structure without any aggregation of gold and/or ruthenium after the photothermal reaction (Supplementary Fig. 15). In addition, due to the high reaction rate and low reaction temperature in our photothermal system, a large amount of water was produced during the reaction. This is undesirable because water condensation can result in the formation of droplets on the quartz window (Supplementary Fig. 27), which could reduce the incident light intensity on the catalyst surface and become the reason

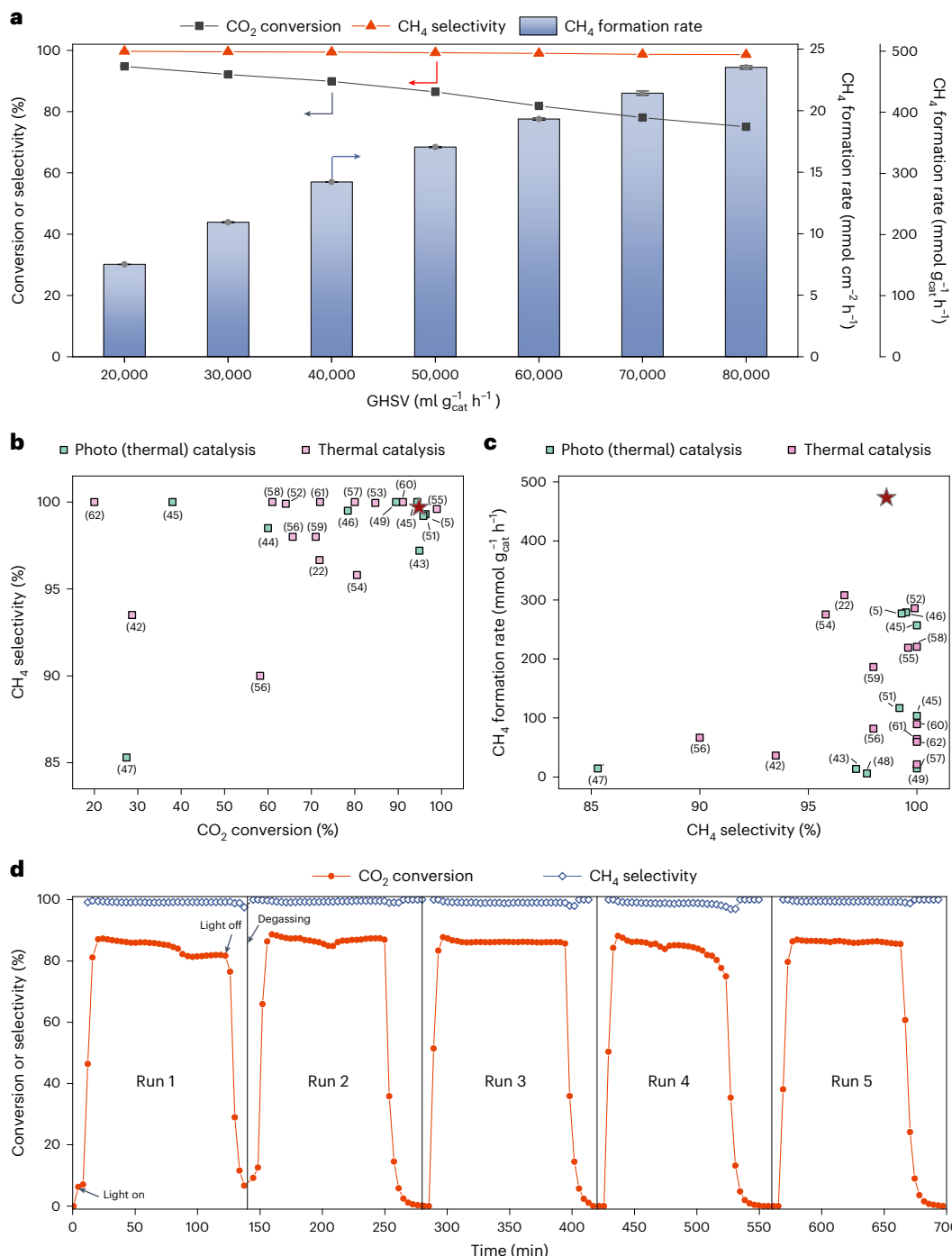


**Fig. 6 | Photothermal CO<sub>2</sub> methanation in a flow reactor.** **a**, Photothermal catalytic activity of Au<sub>0.1</sub>/Ce<sub>0.95</sub>Ru<sub>0.05</sub>O<sub>2</sub> as a function of the GHSV using a concentrated reactant gas. Error bars represent the s.d. based on three measurements. **b,c**, Performance comparison between the current catalyst and previously reported photothermal and thermal catalysts (Supplementary

Tables 4 and 5). Comparison of CH<sub>4</sub> selectivity versus CO<sub>2</sub> conversion (**b**) and comparison of CH<sub>4</sub> formation rate versus CH<sub>4</sub> selectivity (**c**). Stars in **b,c** represent the data reported in this work. The numbers in parentheses are reference numbers. **d**, Catalyst stability in terms of the CO<sub>2</sub> conversion and the CH<sub>4</sub> selectivity.

for the slight decrease of reaction rate in cycles 1 and 4. Therefore, the system was purged with argon gas every 100 min to remove any generated water. From an engineering point of view, it would therefore be desirable to create hydrophobic surfaces on the catalysts and quartz windows that can efficiently remove water from the reactor to prevent water dropping back into the reaction system and shifting the reaction equilibrium toward the reverse reaction. Overall, an excellent CO<sub>2</sub> methanation performance was achieved under mild photothermal

conditions, and our described system shows great potential for use in future practical applications.

To diminish the temperature gradients in catalyst layers for a more accurate comparison of the photothermal catalytic performance under identical reaction conditions, we developed a screen-printing technique<sup>63</sup> for the preparation of thin (20–30 μm) and compact catalyst layers. In brief, we prepared homogeneously dispersed catalyst pastes of Au<sub>0.1</sub>/Ce<sub>0.95</sub>Ru<sub>0.05</sub>O<sub>2</sub> and Ce<sub>0.95</sub>Ru<sub>0.05</sub>O<sub>2</sub>, and screen-printed the pastes

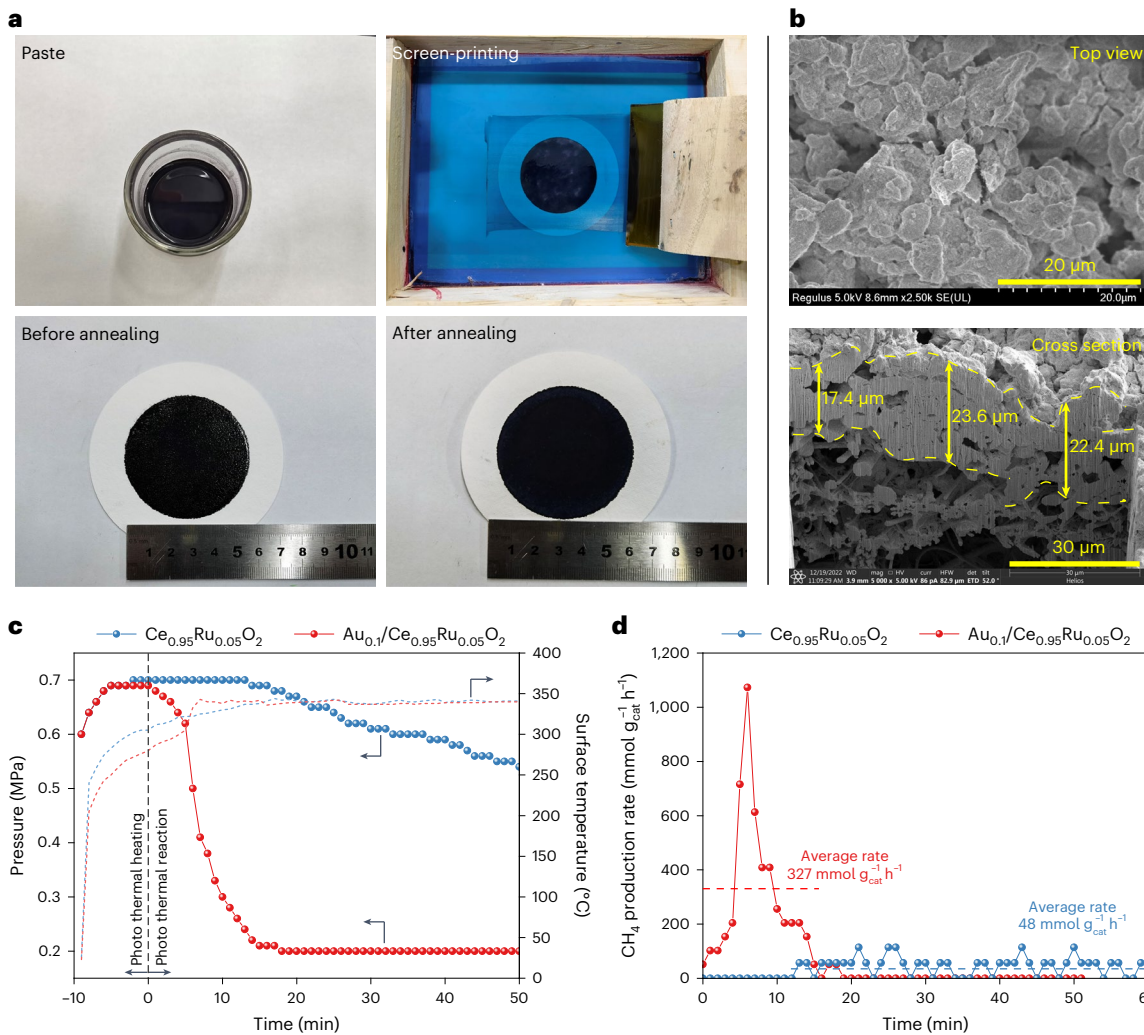


**Fig. 7 | Photothermal  $\text{CO}_2$  methanation on screen-printed catalyst thin layers.**

**a**, Preparation of the thin  $\text{Au}_{0.1}/\text{Ce}_{0.95}\text{Ru}_{0.05}\text{O}_2$  catalyst layers by screen-printing. **b**, SEM image of a thin  $\text{Au}_{0.1}/\text{Ce}_{0.95}\text{Ru}_{0.05}\text{O}_2$  catalyst layer (catalyst loading,  $\sim 4.2 \text{ mg cm}^{-2}$ ). **c,d**, Time-dependent changes in the pressures and surface

temperatures (**c**), and  $\text{CH}_4$  production rates (**d**) in the photothermal batch reaction using the screen-printed  $\text{Ce}_{0.95}\text{Ru}_{0.05}\text{O}_2$  and  $\text{Au}_{0.1}/\text{Ce}_{0.95}\text{Ru}_{0.05}\text{O}_2$  catalysts under 420–780 nm light irradiation.

onto quartz fibre substrates ( $28 \text{ cm}^2$ ) with an 80 mesh screen. After calcination in air at  $450^\circ\text{C}$  for 4 h to fully remove the ethylene cellulose binder, the thin catalyst layers of  $\text{Au}_{0.1}/\text{Ce}_{0.95}\text{Ru}_{0.05}\text{O}_2$  and  $\text{Ce}_{0.95}\text{Ru}_{0.05}\text{O}_2$  were obtained (Fig. 7a,b and Supplementary Fig. 28). Such thin catalyst layers diminished the temperature gradients under light irradiation. The temperature distributions on different catalysts were identical as confirmed by the experimental temperature measurements (Supplementary Figs. 29–30).

We then evaluated the photothermal catalytic performances of the screen-printed catalyst layers ( $4.2 \text{ mg cm}^{-2}$ ) of  $\text{Au}_{0.1}/\text{Ce}_{0.95}\text{Ru}_{0.05}\text{O}_2$  and  $\text{Ce}_{0.95}\text{Ru}_{0.05}\text{O}_2$  (tailed to a 4.2-cm-diameter circle with an area of  $13.8 \text{ cm}^2$ ) using a high-concentration reactant gas (18%  $\text{CO}_2$ , 72%  $\text{H}_2$ , 10% Ar) at an initial pressure of 0.6 MPa in a batch reactor under visible-light irradiation (420–780 nm, CEL-HXF300 xenon lamp). To maintain a constant surface temperature of  $340^\circ\text{C}$  throughout the photothermal catalytic reaction, we adjusted the incident light intensity to be between 16.6 and 28.2 W ( $1.2\text{--}2.0 \text{ W cm}^{-2}$ ). We monitored the temperature using a built-in contact thermocouple attached to the catalyst surface and ensured that both  $\text{Au}_{0.1}/\text{Ce}_{0.95}\text{Ru}_{0.05}\text{O}_2$  and  $\text{Ce}_{0.95}\text{Ru}_{0.05}\text{O}_2$  were subjected to this same condition. It is important to note that because the total number of molecules decreases during  $\text{CO}_2$  methanation, we can directly monitor the pressure change in the batch

reactor to determine the reaction process. Remarkably, as shown in Fig. 7c, the pressure decreased rapidly from 0.7 to 0.2 MPa with the  $\text{Au}_{0.1}/\text{Ce}_{0.95}\text{Ru}_{0.05}\text{O}_2$  catalyst, and the thermodynamic equilibrium was reached within 15 min of commencing the photothermal reaction. In contrast, no pressure change was observed over the initial 15 min for the  $\text{Ce}_{0.95}\text{Ru}_{0.05}\text{O}_2$  catalyst under identical photothermal conditions. After a prolonged 50 min reaction time, the pressure dropped only slightly to 0.5 MPa. This result offered us evidence of the significantly increased photothermal catalytic activity of  $\text{Au}_{0.1}/\text{Ce}_{0.95}\text{Ru}_{0.05}\text{O}_2$  compared with that of  $\text{Ce}_{0.95}\text{Ru}_{0.05}\text{O}_2$ . We also took one-shot videos to record the photothermal reaction and show the greatly improved performance of  $\text{Au}_{0.1}/\text{Ce}_{0.95}\text{Ru}_{0.05}\text{O}_2$  compared with the  $\text{Ce}_{0.95}\text{Ru}_{0.05}\text{O}_2$  catalyst (Supplementary Videos 1 and 2). As shown in Fig. 7d, the average  $\text{CH}_4$  production rate achieved using the screen-printed  $\text{Ce}_{0.95}\text{Ru}_{0.05}\text{O}_2$  catalyst was only  $\sim 48 \text{ mmol g}_{\text{cat}}^{-1} \text{ h}^{-1}$ . In contrast, the average  $\text{CH}_4$  production rate of the screen-printed  $\text{Au}_{0.1}/\text{Ce}_{0.95}\text{Ru}_{0.05}\text{O}_2$  catalyst layer reached  $327 \text{ mmol g}_{\text{cat}}^{-1} \text{ h}^{-1}$  with an  $\sim 93\%$   $\text{CO}_2$  conversion and a  $99\%$   $\text{CH}_4$  selectivity in a batch reactor (Supplementary Table 8), greatly exceeding previous photocatalytic or photothermal catalytic  $\text{CO}_2$  methanation results. In addition, we found that the instantaneous reaction rate reached up to  $\sim 1,100 \text{ mmol g}_{\text{cat}}^{-1} \text{ h}^{-1}$  at the ideal pressure of 0.6 MPa at  $340^\circ\text{C}$  (Fig. 7d) using  $\text{Au}_{0.1}/\text{Ce}_{0.95}\text{Ru}_{0.05}\text{O}_2$ .

## Conclusions

We report here a gold-grafted  $\text{Ce}_{0.95}\text{Ru}_{0.05}\text{O}_2$  solid-solution catalyst ( $\text{Au}/\text{Ce}_{0.95}\text{Ru}_{0.05}\text{O}_2$ ) exhibiting a remarkable photothermal catalytic  $\text{CO}_2$  methanation activity at low operating temperatures approaching the thermal catalysis limit. The role of LSPR hot electrons in promoting photothermal catalysis was evaluated, and it was found that LSPR-induced hot-electron injection from gold to  $\text{Ce}_{0.95}\text{Ru}_{0.05}\text{O}_2$  created large quantities of oxygen vacancies ( $V_{\text{o}}$ ) close to the ruthenium sites, thereby generating an abundance of Ru– $V_{\text{o}}$  active sites for the reaction to take place. In a flow reactor, a high photothermal catalytic  $\text{CH}_4$  formation rate of 473 mmol  $\text{g}_{\text{cat}}^{-1}$   $\text{h}^{-1}$  was achieved at a high GHSV of 80,000 ml  $\text{g}_{\text{cat}}^{-1}$   $\text{h}^{-1}$  and with an ~100%  $\text{CH}_4$  selectivity and an ~75% single-pass  $\text{CO}_2$  conversion under visible–near-infrared light (350–2,500 nm) irradiation without additional heating. Under visible-light irradiation (420–780 nm), the screen-printed  $\text{Au}_{0.1}/\text{Ce}_{0.95}\text{Ru}_{0.05}\text{O}_2$  catalyst exhibited an overall high  $\text{CH}_4$  production rate of 327 mmol  $\text{g}_{\text{cat}}^{-1}$   $\text{h}^{-1}$  with an ~93%  $\text{CO}_2$  conversion and ~100%  $\text{CH}_4$  selectivity in a batch reactor. We expect that our proposed mechanism of plasmonic-steered photochemical and photothermal synergy will contribute greatly to the generation of heterogeneous photochemical and photothermal catalysts for the efficient and high-yield synthesis of valuable carbon-based chemicals. Ongoing research projects in our group are also focusing on solar-driven photosynthetic applications using plasmonic-enhanced, photothermal catalysts for producing  $\text{C}_{2+}$  alkenes and alcohols under commercially relevant operating conditions.

## Methods

### Catalyst preparation

All chemical reagents were purchased from Shanghai Macklin Biochemical. The  $\text{Ce}_{0.95}\text{Ru}_{0.05}\text{O}_2$  and gold-grafted  $\text{Ce}_{0.95}\text{Ru}_{0.05}\text{O}_2$  catalysts were synthesized via co-precipitation followed by hydrothermal crystallization and calcination<sup>64,65</sup>. In the co-precipitation procedure,  $\text{CeCl}_3 \cdot 7\text{H}_2\text{O}$  (3.8 mmol),  $\text{RuCl}_3 \cdot n\text{H}_2\text{O}$  (0.2 mmol) and  $\text{HAuCl}_4 \cdot n\text{H}_2\text{O}$  ( $x$  mmol,  $x = 0, 0.2, 0.3, 0.4, 0.5$  or  $0.6$ ) were dissolved in deionized water (10 ml) and then added dropwise to a 7 mol l<sup>-1</sup> NaOH solution (70 ml) under vigorous stirring to form black precipitate. After ageing for 30 min, the mixture was sealed in a 100 ml polytetrafluoroethylene-lined autoclave and hydrothermally treated at 140 °C for 48 h. Subsequently, the precipitate was collected by centrifugation, washed several times with water and isopropanol, dried at room temperature under vacuum and ground into a fine powder. Finally, the as-synthesized catalyst was obtained by calcination of the powder under air at 400 °C for 4 h. The gold-loaded samples were denoted as  $\text{Au}_m/\text{Ce}_{0.95}\text{Ru}_{0.05}\text{O}_2$  ( $m = 0.05, 0.075, 0.1, 0.125$  or  $0.15$ ). The reference  $\text{CeO}_2$  and  $\text{Au}_{0.1}/\text{CeO}_2$  samples were synthesized following a similar procedure. The preparation of thin catalyst layers by a screen-printing method is described in Supplementary Note 5.

### Photothermal methanation of $\text{CO}_2$

The continuous-flow reaction was performed in a fixed-bed heat chamber (HVC-MRA-5, Harrick Scientific Products) equipped with a quartz window for observation and light irradiation purposes (Supplementary Fig. 1). A cooling-water circulation accessory was connected to the heating chamber to maintain the reactor shell at a low temperature during heat treatment or light irradiation. The catalyst powder was placed in a built-in sample cup and then compressed to a plain surface using a tailored pushrod. A 300 W xenon lamp (CME-303, Microenerg Beijing Technology) equipped with a quartz guidance fibre was used as the light source. A 350 nm long-wave pass filter was installed in the lamp to simulate the solar wavelength distribution (350–2,500 nm). The outlet gas was analysed using an Agilent 990 micro-gas chromatograph equipped with micro-thermal conductivity detectors. The detailed procedures for evaluation of the catalytic performance in a low-concentration gas flow (that is, 4%

$\text{H}_2, 1\% \text{CO}_2$  and 95% Ar) and a high-concentration reactant gas flow (72%  $\text{H}_2$ , 18%  $\text{CO}_2$  and 10% Ar) are described in Supplementary Notes 6 and 7, respectively. The calculation of thermodynamic limits is described in Supplementary Note 8. An adjustable emissivity coaxial laser infrared thermometer (SA-D5050A, Wuxi Shiao) was used to monitor the catalyst surface temperature under light irradiation. The incident light power and irradiance were calibrated by an automatic optical power meter (CEL-NP2000, CEAulight). The emissivity calibration method is described in Supplementary Note 9. The batch reaction was performed in a 100 ml high-pressure stainless reactor (CEL-GPRT100, CEAulight) with a quartz window. A 300 W xenon lamp (CEL-HXF300, CEAulight) was used as the light source. A 420 nm long-wave pass filter and a visible reflection filter (VisREF, 350–780 nm) were installed in the lamp to ensure that the output light was pure visible light (420–780 nm). The catalyst surface temperature was monitored by a built-in thermocouple. The gaseous products in the reactor after a batch reaction were collected in an aluminium foil sampling bag and analysed using the micro-gas chromatograph system. The photothermal batch reactions carried out using the catalyst powders in the low-concentration reactant gas, and the screen-printed catalyst thin layers in the high-concentration reactant gas are described in Supplementary Notes 10 and 11, respectively.

## Characterization

X-ray diffraction patterns were recorded in the  $2\theta$  range of 5°–80° using a Bruker Advance D8 diffractometer with Cu K $\alpha$  radiation and a D/teX Ultra detector. For the gold-grafted sample, the Au(111) diffraction peak was used as an internal standard for correction of the diffraction angles. The SEM images were obtained using a Hitachi Regulus SU8100 instrument at an accelerating voltage of 5 kV, while SEM-EDX analysis was performed using a Zeiss Supra55 instrument at an accelerating voltage of 15 kV. The TEM and STEM images, including EDX mapping, were captured using an FEI TALOS F200X at an accelerating voltage of 200 kV. The ultraviolet–visible–near-infrared DRS was measured using a Shimadzu UV3600Plus spectrometer in the wavelength range 350–2,500 nm with a BaSO<sub>4</sub> reference. XPS analysis under in situ irradiation was carried out using a Thermo Scientific ESCALAB 250Xi spectrometer. EPR signals were collected using a Bruker EMX-plus spectrometer at 77 K, and isotopic tracing was performed using an Ametek Dycor QMS system. The DRIFTS measurement was performed during the light irradiation onto our catalysts using a Fourier transform infrared spectrometer (JASCO, FTIR6100, MCT (HgCdTe) detector) equipped with a temperature-controlled gas-flow chamber (ST Japan). The reaction conditions for measuring the Arrhenius plots were the same as those employed for the performance evaluation of the flow reaction system using a low-concentration reactant gas. Detailed experimental procedures are described in Supplementary Notes 12–15.

## Electromagnetic simulation

Numerical simulations of the extinction spectra for the hybrid systems involving the gold nanoparticles and the  $\text{CeO}_2$  nanorods were performed using commercial software (COMSOL Multiphysics). The diameter of the hyper-hemispherical gold nanoparticles was 12 nm. The  $\text{CeO}_2$  nanorods measured 15 nm × 15 nm × 35 nm. The refractive index of  $\text{CeO}_2$  was obtained from the literature<sup>66</sup>, and the permittivity of gold was obtained from the COMSOL built-in material library. A plane wave was irradiated normally along the negative z-axis direction with x-direction polarization, and the hybrid system was surrounded by a perfectly matched layer condition.

## Data availability

All data are available in the ScienceDB repository at <https://doi.org/10.57760/sciencedb.08102> or from the corresponding author upon reasonable request. Source data are provided with this paper.

## References

1. Wang, W., Wang, S., Ma, X. & Gong, J. Recent advances in catalytic hydrogenation of carbon dioxide. *Chem. Soc. Rev.* **40**, 3703–3727 (2011).
2. Global Roadmap for Implementing CO<sub>2</sub> Utilization (Global CO<sub>2</sub> Initiative, 2019); <http://deepblue.lib.umich.edu/handle/2027.42/150624>
3. Bailera, M., Lisbona, P., Romeo, L. M. & Espatolero, S. Power to gas projects review: lab, pilot and demo plants for storing renewable energy and CO<sub>2</sub>. *Renew. Sustain. Energy Rev.* **69**, 292–312 (2017).
4. Wulf, C., Linßen, J. & Zapp, P. Review of power-to-gas projects in Europe. *Energy Procedia* **155**, 367–378 (2018).
5. Ren, J. et al. Targeting activation of CO<sub>2</sub> and H<sub>2</sub> over Ru-loaded ultrathin layered double hydroxides to achieve efficient photothermal CO<sub>2</sub> methanation in flow-type system. *Adv. Energy Mater.* **7**, 1601657 (2017).
6. Li, Y. et al. Selective light absorber-assisted single nickel atom catalysts for ambient sunlight-driven CO<sub>2</sub> methanation. *Nat. Commun.* **10**, 2359 (2019).
7. Chen, Y. et al. Cooperative catalysis coupling photo-/photothermal effect to drive Sabatier reaction with unprecedented conversion and selectivity. *Joule* **5**, 3235–3251 (2021).
8. Chen, G. et al. Alumina-supported CoFe alloy catalysts derived from layered-double-hydroxide nanosheets for efficient photothermal CO<sub>2</sub> hydrogenation to hydrocarbons. *Adv. Mater.* **30**, 1704663 (2018).
9. Li, Z. et al. Fe-based catalysts for the direct photohydrogenation of CO<sub>2</sub> to value-added hydrocarbons. *Adv. Energy Mater.* **11**, 2002783 (2021).
10. Kong, N. et al. Ruthenium nanoparticles supported on Mg(OH)<sub>2</sub> microflowers as catalysts for photothermal carbon dioxide hydrogenation. *ACS Appl. Nano Mater.* **3**, 3028–3033 (2020).
11. Wu, Z. et al. Niobium and titanium carbides (MXenes) as superior photothermal supports for CO<sub>2</sub> photocatalysis. *ACS Nano* **15**, 5696–5705 (2021).
12. Li, X., Zhang, X., Everitt, H. O. & Liu, J. Light-induced thermal gradients in ruthenium catalysts significantly enhance ammonia production. *Nano Lett.* **19**, 1706–1711 (2019).
13. Brongersma, M. L., Halas, N. J. & Nordlander, P. Plasmon-induced hot carrier science and technology. *Nat. Nanotechnol.* **10**, 25–34 (2015).
14. Robatjazi, H. et al. Plasmon-induced selective carbon dioxide conversion on earth-abundant aluminum-cuprous oxide antenna-reactor nanoparticles. *Nat. Commun.* **8**, 27 (2017).
15. Zhang, X. et al. Product selectivity in plasmonic photocatalysis for carbon dioxide hydrogenation. *Nat. Commun.* **8**, 14542 (2017).
16. Wei, Q., Wu, S. & Sun, Y. Quantum-sized metal catalysts for hot-electron-driven chemical transformation. *Adv. Mater.* **30**, 1802082 (2018).
17. Aslam, U., Rao, V. G., Chavez, S. & Linic, S. Catalytic conversion of solar to chemical energy on plasmonic metal nanostructures. *Nat. Catal.* **1**, 656–665 (2018).
18. Jiang, H. et al. Synergistic photothermal and photochemical partial oxidation of methane over noble metals incorporated in mesoporous silica. *Chem. Commun.* **55**, 13765–13768 (2019).
19. Jiang, H. et al. Photocatalytic partial oxidation of methane on palladium-loaded strontium tantalate. *Sol. RRL* **3**, 1900076 (2019).
20. Sun, Y. & Tang, Z. Photocatalytic hot-carrier chemistry. *MRS Bull.* **45**, 20–25 (2020).
21. Chapkin, K. D. et al. Lifetime dynamics of plasmons in the few-atom limit. *Proc. Natl Acad. Sci. USA* **115**, 9134–9139 (2018).
22. Jia, X., Zhang, X., Rui, N., Hu, X. & Liu, C. Structural effect of Ni/ZrO<sub>2</sub> catalyst on CO<sub>2</sub> methanation with enhanced activity. *Appl. Catal. B Environ.* **244**, 159–169 (2019).
23. Gordon, S. & McBride, B. J. *Computer Program for Calculation of Complex Chemical Equilibrium Compositions and Applications. Part 1: Analysis* (NASA, 1994).
24. Yu, Y., Williams, J. D. & Willets, K. A. Quantifying photothermal heating at plasmonic nanoparticles by scanning electrochemical microscopy. *Faraday Discuss.* **210**, 29–39 (2018).
25. Jiang, Q., Rogez, B., Claude, J.-B., Baffou, G. & Wenger, J. Temperature measurement in plasmonic nanoapertures used for optical trapping. *ACS Photonics* **6**, 1763–1773 (2019).
26. Wang, Q.-Y. et al. Instantly detecting catalysts' hot spots temperature in situ during photocatalysis by operando Raman spectroscopy. *Anal. Chem.* **93**, 15517–15524 (2021).
27. Shannon, R. D. Revised effective ionic radii and systematic studies of interatomic distances in halides and chalcogenides. *Acta Crystallogr. A* **32**, 751–767 (1976).
28. Xie, X., Li, Y., Liu, Z.-Q., Haruta, M. & Shen, W. Low-temperature oxidation of CO catalysed by Co<sub>3</sub>O<sub>4</sub> nanorods. *Nature* **458**, 746–749 (2009).
29. Ge, H., Kuwahara, Y., Kusu, K. & Yamashita, H. Plasmon-induced catalytic CO<sub>2</sub> hydrogenation by a nano-sheet Pt/H<sub>x</sub>MoO<sub>3-y</sub> hybrid with abundant surface oxygen vacancies. *J. Mater. Chem. A* **9**, 13898–13907 (2021).
30. Bushira, F. A. et al. Plasmon-boosted Cu-doped TiO<sub>2</sub> oxygen vacancy-rich luminol electrochemiluminescence for highly sensitive detection of alkaline phosphatase. *Anal. Chem.* **93**, 15183–15191 (2021).
31. Li, Y. et al. Plasmonic hot electrons from oxygen vacancies for infrared light-driven catalytic CO<sub>2</sub> reduction on Bi<sub>2</sub>O<sub>3-x</sub>. *Angew. Chem. Int. Ed.* **60**, 910–916 (2021).
32. Liu, X., Dong, G., Li, S., Lu, G. & Bi, Y. Direct observation of charge separation on anatase TiO<sub>2</sub> crystals with selectively etched {001} facets. *J. Am. Chem. Soc.* **138**, 2917–2920 (2016).
33. Gassman, P. G. & Winter, C. H. Preparation, electrochemical oxidation, and XPS studies of unsymmetrical ruthenocenes bearing the pentamethylcyclopentadienyl ligand. *J. Am. Chem. Soc.* **110**, 6130–6135 (1988).
34. Soria, J., Conesa, J. C. & Martínez-Arias, A. Characterization of surface defects in CeO<sub>2</sub> modified by incorporation of precious metals from chloride salts precursors: an EPR study using oxygen as probe molecule. *Colloids Surf. A* **158**, 67–74 (1999).
35. Shoji, S. et al. Photocatalytic uphill conversion of natural gas beyond the limitation of thermal reaction systems. *Nat. Catal.* **3**, 148–153 (2020).
36. Sharma, S. et al. Mechanistic insights into CO<sub>2</sub> methanation over Ru-substituted CeO<sub>2</sub>. *J. Phys. Chem. C* **120**, 14101–14112 (2016).
37. Wang, F. et al. Active site dependent reaction mechanism over Ru/CeO<sub>2</sub> catalyst toward CO<sub>2</sub> methanation. *J. Am. Chem. Soc.* **138**, 6298–6305 (2016).
38. Furube, A., Du, L., Hara, K., Katoh, R. & Tachiya, M. Ultrafast plasmon-induced electron transfer from gold nanodots into TiO<sub>2</sub> nanoparticles. *J. Am. Chem. Soc.* **129**, 14852–14853 (2007).
39. Du, L. et al. Plasmon-induced charge separation and recombination dynamics in gold-TiO<sub>2</sub> nanoparticle systems: dependence on TiO<sub>2</sub> particle size. *J. Phys. Chem. C* **113**, 6454–6462 (2009).
40. Mukherjee, S. et al. Hot electrons do the impossible: plasmon-induced dissociation of H<sub>2</sub> on Au. *Nano Lett.* **13**, 240–247 (2013).
41. Swearer, D. F. et al. Heterometallic antenna-reactor complexes for photocatalysis. *Proc. Natl Acad. Sci. USA* **113**, 8916–8920 (2016).
42. Fan, M. et al. Atomic Ru immobilized on porous h-BN through simple vacuum filtration for highly active and selective CO<sub>2</sub> methanation. *ACS Catal.* **9**, 10077–10086 (2019).
43. Sastre, F., Puga, A. V., Liu, L., Corma, A. & García, H. Complete photocatalytic reduction of CO<sub>2</sub> to methane by H<sub>2</sub> under solar light irradiation. *J. Am. Chem. Soc.* **136**, 6798–6801 (2014).

44. Jantarang, S. et al. Altering the influence of ceria oxygen vacancies in Ni/Ce<sub>x</sub>Si<sub>y</sub>O<sub>2</sub> for photothermal CO<sub>2</sub> methanation. *Catal. Sci. Technol.* **11**, 5297–5309 (2021).
45. Mateo, D. et al. Efficient visible-light driven photothermal conversion of CO<sub>2</sub> to methane by nickel nanoparticles supported on barium titanate. *Adv. Funct. Mater.* **31**, 2008244 (2021).
46. Li, Z., Shi, R., Zhao, J. & Zhang, T. Ni-based catalysts derived from layered-double-hydroxide nanosheets for efficient photothermal CO<sub>2</sub> reduction under flow-type system. *Nano Res.* **14**, 4828–4832 (2021).
47. He, Z.-H. et al. Photothermal CO<sub>2</sub> hydrogenation to hydrocarbons over trimetallic Co–Cu–Mn catalysts. *Green. Chem.* **23**, 5775–5785 (2021).
48. Chen, X. et al. MOF-templated preparation of highly dispersed Co/Al<sub>2</sub>O<sub>3</sub> composite as the photothermal catalyst with high solar-to-fuel efficiency for CO<sub>2</sub> methanation. *ACS Appl. Mater. Interfaces* **12**, 39304–39317 (2020).
49. Mateo, D., Albero, J. & García, H. Titanium-perovskite-supported RuO<sub>2</sub> nanoparticles for photocatalytic CO<sub>2</sub> methanation. *Joule* **3**, 1949–1962 (2019).
50. Jelle, A. A. et al. Highly efficient ambient temperature CO<sub>2</sub> photomethanation catalyzed by nanostructured RuO<sub>2</sub> on silicon photonic crystal support. *Adv. Energy Mater.* **8**, 1702277 (2018).
51. Meng, X. et al. Photothermal conversion of CO<sub>2</sub> into CH<sub>4</sub> with H<sub>2</sub> over group VIII nanocatalysts: an alternative approach for solar fuel production. *Angew. Chem. Int. Ed.* **53**, 11478–11482 (2014).
52. Aziz, M. A. A. et al. Highly active Ni-promoted mesostructured silica nanoparticles for CO<sub>2</sub> methanation. *Appl. Catal. B* **147**, 359–368 (2014).
53. Do, J. Y. et al. Effective thermocatalytic carbon dioxide methanation on Ca-inserted NiTiO<sub>3</sub> perovskite. *Fuel* **271**, 117624 (2020).
54. Ye, R.-P. et al. High-performance of nanostructured Ni/CeO<sub>2</sub> catalyst on CO<sub>2</sub> methanation. *Appl. Catal. B* **268**, 118474 (2020).
55. Bukhari, S. N. et al. Optimal Ni loading towards efficient CH<sub>4</sub> production from H<sub>2</sub> and CO<sub>2</sub> over Ni supported onto fibrous SBA-15. *Int. J. Hydrog. Energy* **44**, 7228–7240 (2019).
56. Li, J. et al. Enhanced CO<sub>2</sub> methanation activity of Ni/anatase catalyst by tuning strong metal-support interactions. *ACS Catal.* **9**, 6342–6348 (2019).
57. Chai, S. et al. Boosting CO<sub>2</sub> methanation activity on Ru/TiO<sub>2</sub> catalysts by exposing (001) facets of anatase TiO<sub>2</sub>. *J. CO<sub>2</sub> Util.* **33**, 242–252 (2019).
58. Zhang, L., Bian, L., Zhu, Z. & Li, Z. La-promoted Ni/Mg-Al catalysts with highly enhanced low-temperature CO<sub>2</sub> methanation performance. *Int. J. Hydrog. Energy* **43**, 2197–2206 (2018).
59. Mutz, B. et al. Potential of an alumina-supported Ni<sub>3</sub>Fe catalyst in the methanation of CO<sub>2</sub>: impact of alloy formation on activity and stability. *ACS Catal.* **7**, 6802–6814 (2017).
60. Zhou, G. et al. Role of surface Ni and Ce species of Ni/CeO<sub>2</sub> catalyst in CO<sub>2</sub> methanation. *Appl. Surf. Sci.* **383**, 248–252 (2016).
61. Rahmani, S., Rezaei, M. & Meshkani, F. Preparation of highly active nickel catalysts supported on mesoporous nanocrystalline γ-Al<sub>2</sub>O<sub>3</sub> for CO<sub>2</sub> methanation. *J. Ind. Eng. Chem.* **20**, 1346–1352 (2014).
62. Tada, S., Ochieng, O. J., Kikuchi, R., Haneda, T. & Kameyama, H. Promotion of CO<sub>2</sub> methanation activity and CH<sub>4</sub> selectivity at low temperatures over Ru/CeO<sub>2</sub>/Al<sub>2</sub>O<sub>3</sub> catalysts. *Int. J. Hydrog. Energy* **39**, 10090–10100 (2014).
63. Kujirai, T., Yamaguchi, A., Fujita, T., Abe, H. & Miyauchi, M. Active site separation of photocatalytic steam reforming of methane using a gas-phase photoelectrochemical system. *Chem. Commun.* **57**, 8007–8010 (2021).
64. Chen, Y. et al. A robust fuel cell operated on nearly dry methane at 500 °C enabled by synergistic thermal catalysis and electrocatalysis. *Nat. Energy* **3**, 1042–1050 (2018).
65. Guo, Y. et al. Low-temperature CO<sub>2</sub> methanation over CeO<sub>2</sub>-supported Ru single atoms, nanoclusters, and nanoparticles competitively tuned by strong metal-support interactions and H-spillover effect. *ACS Catal.* **8**, 6203–6215 (2018).
66. Goubin, F. et al. Experimental and theoretical characterization of the optical properties of CeO<sub>2</sub>, SrCeO<sub>3</sub>, and Sr<sub>2</sub>CeO<sub>4</sub> containing Ce<sup>4+</sup> (f<sub>0</sub>) ions. *Chem. Mater.* **16**, 662–669 (2004).

## Acknowledgements

This work was supported by the National Natural Science Foundation of China (grant numbers 22272078, 91963121), the National Key Research and Development Program of the Ministry of Science and Technology of China (number 2020YFA0406102), and the Frontiers Science Center for Critical Earth Material Cycling of Nanjing University.

## Author contributions

M.Z. supervised the project and conceived the idea. M.Z. and H.J. designed the experiments. H.J. and L.W. performed the synthesis, characterizations and performance tests. R.G. and W.D. provided the apparatus and helped perform the isotopic tracer analysis. H.K., A.Y. and M.M. reproduced the photothermal catalytic performance and carried out operando DRIFTS measurement. H.S. provided the apparatus and helped perform the EPR and ultraviolet-visible-near-infrared DRS tests. G.S. conducted the electromagnetic simulations. G.S., L.L., J.Z., F.Z., F.L., M.M., W.D. and M.Z. discussed the experimental results. H.J., G.S., A.Y., M.M., W.D. and M.Z. wrote the manuscript. All authors discussed the results and assisted during manuscript preparation.

## Competing interests

The authors declare no competing interests.

## Additional information

**Supplementary information** The online version contains supplementary material available at <https://doi.org/10.1038/s41929-023-00970-z>.

**Correspondence and requests for materials** should be addressed to Miao Zhong.

**Peer review information** *Nature Catalysis* thanks Agustin Bueno Lopez and Emiliano Cortés for their contribution to the peer review of this work.

**Reprints and permissions information** is available at [www.nature.com/reprints](http://www.nature.com/reprints).

**Publisher's note** Springer Nature remains neutral with regard to jurisdictional claims in published maps and institutional affiliations.

Springer Nature or its licensor (e.g. a society or other partner) holds exclusive rights to this article under a publishing agreement with the author(s) or other rightsholder(s); author self-archiving of the accepted manuscript version of this article is solely governed by the terms of such publishing agreement and applicable law.

© The Author(s), under exclusive licence to Springer Nature Limited 2023